Discover Mechanical Engineering

Discover

Research

Modification of 316L steel powders with bronze using high energy ball milling for use as a binder component in PBF-LB/M printing of diamond-metal matrix composites

Wolfgang Tillmann[1] · **Manuel Pinho Ferreira**[1]

Received: 11 August 2023 / Accepted: 9 October 2023
Published online: 17 October 2023

Abstract
For the processing of diamond-metal matrix composites, the powder bed fusion using a laser for metals (PBF-LB/M), represents a new promising method for the additive manufacturing of diamond tools for concrete and rock machining, even with more complicated geometries. Previous research activities show a strong tendency for cracking and delamination during the construction process of the samples. This behavior is caused by thermal residual stresses associated with the embedded diamonds. To control these negative effects on the process side, the volume energy density is reduced accordingly, which, however, led to increased pore formation. This publication deals with an approach on the material side to modify a 316L stainless steel base powder with an addition of 20 wt% bronze via a high energy ball milling (HEBM) process in such a way that a homogeneous solid solution phase is created. A significantly increasing of the melting interval and a decreasing of both solidus and liquidus temperature was observed, which can reduce pore formation in the PBF-LB/M-process. In addition, XRD-diffractometry and SEM/EDS-analysis showed that the homogeneous solid solution phase of this alloyed powder segregates again into Fe- and Cu-rich phases when heated up to the melting point.

Keywords High energy ball milling · Mechanical alloying · 316L-steel/bronze alloy · Metastable phases · Reduced melting range · Segregation of Cu-phases

1 Introduction

1.1 Powder bed fusion using a laser for metals (PBF-LB/M) of diamond metal composites

Additive manufacturing for the fabrication of diamond-metal-matrix composites (DMMC) for natural stone and concrete machining [1–4] using PBF-LB/M is still a challenge, both in terms of process and materials. Among other things, the high cooling rate during the laser melting process leads to thermal residual stresses in the component. In conjunction with the metal-diamond material pairing and their different coefficients of thermal expansion, these residual stresses, which always occur in the PBF-LB/M process anyway, lead to severe cracking and delamination [5–7]. Another problem is the high heat input induced by the laser and the associated thermal attack of the diamonds. Since diamond is the metastable modification of carbon, interfacial reactions take place at the diamond surface at higher temperatures, especially in the presence of reactive transition metals, which leads to the transformation to graphite and thus to the impairment of the

✉ Manuel Pinho Ferreira, manuel.ferreira@tu-dortmund.de; Wolfgang Tillmann, wolfgang.tillmann@tu-dortmund.de | [1]Institute of Materials Engineering, TU-Dortmund, Leonhard-Euler-Str. 2, Dortmund 44227, NRW, Germany.

cutting performance of the diamonds in the tool [8–11]. On the process side, these negative influences of the PBF-LB/M process on the DMMC properties can certainly be achieved by reducing the volume energy density. However, a reduction in the energy transferred to the powder bed leads to incomplete melting of the powder and therefore to high porosity and increased accumulation of diamond particles in the pore spaces [7, 12]. Accordingly, the process parameters must be well chosen to achieve an optimum intermediate between low thermal residual stresses and high relative density.

Now, in order to be more independent of higher volume energy densities to obtain high-density and crack-free DMMC components, this work will investigate a material-side approach to reduce the melting temperature of the metallic binder. The approach taken here is to mechanically alloy a 316L steel powder used for the production of diamond-metal composites with a low-melting tin bronze by means of a high-energy milling process. Previous research activities regarding the use of powder blends to produce compositionally-tailored materials in the PBF 3D printing process have been carried out so far, for example, by Ron et al. and Koptyug et al. The research topics of these works dealt with the in-situ alloy formation of metal powder mixtures during an electron beam or laser beam based PBF process. It was shown that alloy formation and homogenization is possible for various steel-based powder mixtures as well as for a refractory metal HEA powder mixture [13, 14]. The results presented in this paper also deal with the tailoring of metal powders for a PBF process, but vary in approach and basic idea from the previously mentioned publications. The aim is to modify a common steel powder (316L) by means of mechanical alloying in such a way that a lower melting point and liquid phase formation during the PBF-L/M process result in more advantageous material properties when used as a binder metal for DMMC materials.

The use of an iron-based alloy (316L) for the production of DMMCs is based on current trends to reduce the use of so-called critical raw materials (CRMs). With regard to diamond-metal composites, mainly cobalt-based metal binders have been used in the past. Due to significant market price fluctuations and the general increase in the price of cobalt, as well as its toxic properties, measures were taken in the early 2000s to continuously replace cobalt with other non-problematic metals (e.g.: iron) [15–17]. On the other hand the use of CuSn as an alloy component is due to the fact that in the conventional production of diamond-metal composites by sintering, the admixture of low-melting materials such as copper or bronze is state of the art [3, 4, 18, 19].

1.2 High energy milling and nanocrystalline/amorphous metals

High energy milling of metallic powder mixtures has established itself as a reliable technique to alloy a wide range of elemental components [20–24]. The advantage of this type of homogenization and mixing is due to the fact that the process takes place in the solid phase of all powder components. Thus, the high costs but also the negative material-technical effects of melt metallurgy can be circumvented. The structural properties of the high-energy milled end products are very different. Depending on the starting products used and the milling parameters, both crystalline structures and amorphous solid phases can be produced. With regard to the production of solid solution powders, high-energy milling is preferred for the production of high entropy alloys (HEA). After complete mechanical alloying, the resulting HEA powders in most cases have a body-centered cubic or face-centered cubic crystal lattice with a nanoscale microstructure but still a clearly crystalline state [22, 25, 26]. Furthermore, the positive effect of high energy ball milling (HEBM) on the corrosion and material properties of age hardening aluminum alloys such as AA2024, AA6061 and AA7075 was investigated. Here, transmission electron microscopy was able to detect grain refinement in the metal structure below 100 nm. At the same time, the solid phase solubility expanded with a suppression of the formation of intermetallic phases, which may indicate a gradual transition from a stable crystalline state to a metastable amorphous state [27].

In the application area of amorphous/nanocrystalline Fe-Si-B-P-Cu composites with soft magnetic properties, conventional manufacturing methods such as, in particular, single roller melt-spinning have been established so far. The amorphous ribbons produced by this process were subsequently heat treated to selectively control the formation of nanocrystallites [28, 29]. Regarding the same material composition, Motozuka et al. [30] determined that the amorphous and nanocrystalline structures were very well preserved by a high-energy milling process and at the same time could be easily processed from alloy scrap into a powder. Likewise, a reduction in the intensity of the X-rays reflected from the α -Fe-phase compared to the initial state was measured for ball-milled samples on the basis of XRD spectra.

The generation of high proportions of amorphous and nanocrystalline phases in metallic alloys by means of HEBM is the subject of numerous research activities. In particular, the ternary aluminum-based alloys ($Al_{65}Cu_{20}TM_{15}$ with TM=Ti, Nb, Zr) should be mentioned, with which amorphous alloys could be produced by means of mechanical alloying (HEBM) from a milling time of 30 to 50 hours in which nanocrystalline phases are dispersed [31–33]. Ternary, quaternary and quinary zirconium-based alloys (for example: Zr–Cu–Al; $Zr_{65}Cu_{17,5}Ni_{10}Al_{7,5}$; $Zr_{57}Ti_5Cu_{20}Ni_8Al_{10}$) behave similar in a HEBM

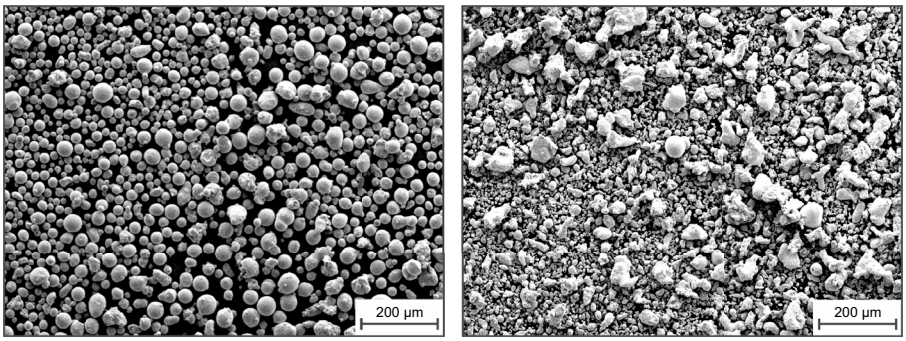

(a) Steel-Powder (b) Bronze-Powder

Fig. 1 SEM-pictures of the feedstock materials

Table 1 Elemental composition of the feedstock

Steel (316L)		Bronze	
wt%		wt%	
C	0.03	Cu	90.0
Si	1.0	Sn	10.0
Mn	1.0		
Cr	17.0		
Ni	13.0		
Mo	2.0		
Fe	Balance		

mechanical alloying process with high grinding times. Here, an almost complete amorphization could be observed in approx. 20 to 60 hours. In the case of the quinary titanium-base alloy due to the addition of glass-forming compounds, the grinding time could even be reduced to about 2 to 8 hours [34–36]. Finally, the ternary TiNiNb and binary $Ti_{50}Fe_{50}$ alloys should also be mentioned, where even near complete amorphization could be achieved within 50 to 75 h [37, 38].

Based on the presented research activities in the field of mechanical alloying of metal powders using HEBM, the following work will investigate the realization of a mechanical alloying process of a 316L steel/bronze mixture. Since the main constituents Fe and Cu have low solubility in each other in the solid phase, the miscibility in presence of the alloy constituents (see Table 1) in the stainless steel (316L) and the tin bronze (Cu90Sn10) during mechanical alloying will be investigated in particular. The focus will also be on the formation of metastable forced-dissolved or nanocrystalline/amorphous phases. Finally, it will be verified whether the application-oriented goal of lowering the melting point of the steel powder for an PBF-LB/M process can be achieved and, furthermore, what the thermal properties of the resulting HEBM powder are.

2 Methods

2.1 Used materials and mechanical alloying

The feedstock materials used for the milling experiments are a 316L stainless steel powder and a bronze powder commonly used as a liquid-phase forming component for DMMCs. According to the manufacturer, the steel powder is fabricated by gas atomization and has a spherical grain shape with a grain size of 10 µm to 53 µm (Fig. 1a) and a relatively low fine particle content, which makes it suitable for PBF-LB/M processes in this respect (Fig. 4a). In contrast, the bronze powder is fabricated by water atomization and has an irregular grain shape with a grain size of < 63 µm (Fig. 1b). All grinding tests were performed with a steel/bronze mixture in a mass ratio of 80/20. The exact chemical composition of both metal powders is shown in Table 1.

All milling processes were done in a fully programmable ball mill that can be operated up to a maximum rotational speed of 400 rpm. In addition, it is possible to carry out the milling process in interval operation with or without direction

reversal. Interval operation means that the system can be set so that a defined rotation time and a defined pause time take place in permanent alternation. A total of four containers with a volume of 12 mL to 500 mL can be placed in the ball mill. However, for the experiments described in this paper, only two 250 mL containers made of hardened steel were used. The milling balls used are made of 100Cr6 bearing steel and are weighed in at a ball-to-powder ratio (BPR) of 10:1 for all tests. This means that in absolute values per grinding container, the total initial weight of the steel/bronze mixture was 50 g and the total initial weight of grinding balls was 500 g accordingly. In order to achieve an optimum balance between powder refinement and cold welding during the milling process, 1.5 wt% (0.75 g) stearic acid in powder form was added to the feedstock as a milling additive. These mentioned milling parameters and weights were kept constant for all mechanical alloying processes for unambiguous reproducibility. In contrast, the machine parameters that have a direct effect on the HEBM process were adjusted. These include the rotational speed, the milling time and the activation of the already described interval operation with direction reversal (Table 2).

To avoid disruptive oxidation during the grinding process, both vessels were purged with argon for 30 s and then sealed at an argon overpressure of e5 Pa.

2.2 Optical microscopy and scanning electron microscopy with EDS

Depending on the milling parameters described in Sect. 2.1, the resulting mechanically alloyed steel/bronze powders were evaluated using a reflected light microscope at a magnification of 25× to 100×. Accordingly, embedded and metallographically prepared (grinding and polishing) powder samples were examined after the grinding process for the existence of reddish separately present bronze particles and heterogeneous or non-mixed bronze-rich areas in the steel particles. If these bronze-containing clusters can be detected in the powder samples, then it is a case of an incomplete mechanical alloying process. If, however, no red bronze areas can be detected in the milled steel powder samples, then a complete alloying process can be assumed.

A field emission scanning electron microscope (SEM) with an attached energy dispersive X-ray spectrometer (EDS) was used to analyze grain geometry and grain morphology, and to quantitatively determine the elemental composition. In addition to the embedded and prepared powder samples from the optical microscopy analyses, loose powders were also examined for the SEM studies. The electron micrographs were taken at an accelerating voltage of 20 kV. The working distance was approximately 9 mm to 12 mm and the magnification was selected between 50× and 1000×, depending on the requirements. In addition, it was possible to switch between a secondary electron (topography contrast) and a backscattered electron detector (material contrast). Quantitative elemental analysis using the EDS system was also performed at 20 kV. Only the beam current of the electron microscope had to be increased to a maximum of 16, as required, in order to be able to detect a sufficiently high intensity of X-rays.

2.3 Powder analyses

In order to assess the processability of the high energy milled powder samples in a future PBF-LB/M process at this early stage, the dynamic flowability was determined at the macroscopic level. For this purpose, the respective powder samples were filled into a narrow drum with two glass discs (approx. 25 g to 30 g). During the measurement, the drum rotates and a CCD camera records images of the powder as a film. Via online image analysis, avalanche energy and avalanche angle of the moving powder surface are automatically recorded. For each powder sample, both parameters were determined at rotation speeds of 0.3 rpm, 0.5 rpm and 1.0 rpm, and the average values were calculated.

Table 2 Variable milling parameters

Parameter	Values
Rotational speed [rpm]	250/300/350/400
Milling time [h]	6/12/24/36/48/72
Interval operation	Yes/no
Interval time [h]	1 (a total of x hours pause time + x hours milling time)
Direction reversal	Always during interval operation

In addition, at the microscopic level, the grain size distribution of the powders in the milled and unsieved states was measured by laser diffraction in a liquid suspension in order to determine, among other things, the fine grain content after the HEBM process and thus estimate the usefulness of the metal powder in the PBF-LB/M process.

2.4 X-ray diffraction (XRD)

To investigate the crystalline properties of the mechanically alloyed powder samples, an X-ray diffractometer with the Bragg-Brentano arrangement and the (θ-θ)-geometry was used. In particular, the milled powders were analyzed as a function of the grinding time. As a reference, in addition to the diffractograms of the pure starting materials (316L and bronze), the diffraction spectrum of a steel-bronze powder fraction (80/20 wt%) mixed in a tumbling mixer for one hour was used. The diffraction pattern of the mixed powder components was mainly used to compare the crystalline structure of the milled powder with the structure of non-milled and consequently non-mechanically alloyed steel-bronze powders. In this respect, the main aim is to draw conclusions about the formation of stable or metastable solid solutions formed from the two starting substances. In addition, the mechanically alloyed powders are investigated for the formation of new phases and the emergence of amorphous and nanocrystalline structures during the milling process.

To ensure comparability, all measurements were performed with a Cu-K_α X-ray tube and an attached 2 mm polycapillary. The detector is based on the 1-dimensional compound silicon strip technology. The 2θ range between 20° to 120°, a stepsize of 0.05° and a time per step of 1.0 s were used as measurement parameters. The total measuring time was therefore ~40 min per powder sample.

2.5 Differential thermal analysis (DTA)

In order to analyze the thermal behavior of the mechanically alloyed powders during heating, especially near the melting range, a DTA/DSC combination instrument was used. However, since in this work the focus is on the detection of the melting areas, but also on phase changes of the modified milled powders, differential calorimetry and the associated measurement of the heat flux (mW) are not used and only the thermoelectric voltage difference (µV) is included as a measured value. In order to verify the described primary objective of lowering the melting point of the steel powders mechanically alloyed with bronze, the melting peaks of the DTA curves are evaluated with respect to the onset and the offset of the melting peak, which corresponds to the approximate solidus or liquidus temperature. These characteristic material values are compared with those of pure 316L steel powder. Furthermore, temperature-dependent phase transitions and the formation of new phases are to be detected by means of this measurement method. All DTA-analyses were performed in each case in an alumina sample crucible. An empty alumina crucible was used as a reference. The temperature profile consisted of first heating up to 1550 °C at a heating rate of 10 K min^{-1}, holding at this temperature for 5 min and then specifically cooling down again at 10 K min^{-1} to 100 °C. The measurements were always performed under an argon flow of 1.5 L min^{-1} to avoid oxidation. At the beginning of the measurements and after every fifth sample, a zero measurement was performed with an empty sample crucible and an empty reference crucible under the same conditions to compensate for the device-specific error. The transfer of the measurement data to the PC was carried out with a sampling interval of 1 s in a measurement range of 250 µV.

2.6 Heat treatment and remelting

Heat treatment of the mechanically alloyed steel/bronze powder was performed to further investigate the exothermic reaction occurring in the temperature range of 550 °C to 650 °C in the DTA measurement (Sect. 3.4). For this purpose, a small amount of about 5 g of the powder samples from the HEBM tests was aged in a vacuum chamber furnace at a pressure of e-3 Pa at 700 °C for 30 min. The powder samples treated in this way are then examined in the X-ray diffraction apparatus for changes in structural properties as well as the formation of new phases, and compared with the alloyed powders in the previous condition.

Parallel, the remelted mechanically alloyed samples from the DTA tests were examined under a scanning electron microscope and in a X-ray diffractometer for individual components and phases in the solidified microstructure in order to obtain conclusions about the melting behavior of the milled powders.

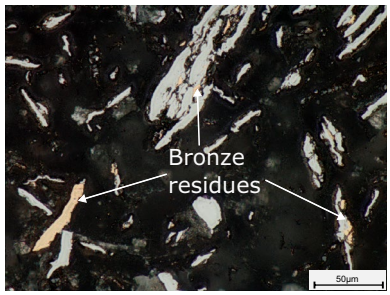

(a) Optical microscopy of mechanically alloyed powder with 300 rpm for 6 h

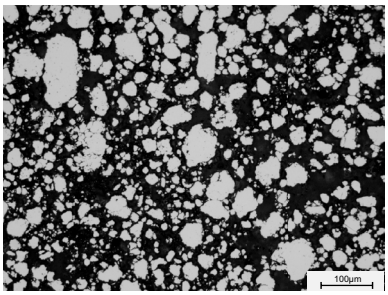

(b) Optical microscopy of mechanically alloyed powder with 300 rpm for 12 h

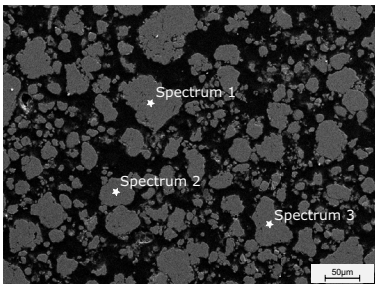

(c) SEM microscopy of mechanically alloyed powder with 300 rpm for 12 h (with EDS measuring points)

Fig. 2 Investigation of the homogenization process

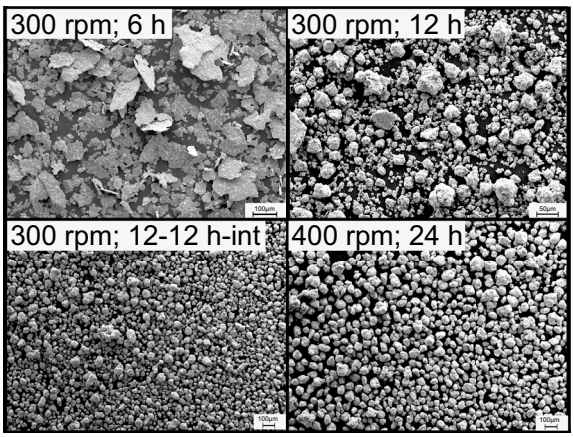

Fig. 3 Grain morphology and grain size distribution as a function of grinding parameters

3 Results and discussion

3.1 Homogenization and grain morphology

The first investigations, which concerned the mechanically alloyed powder, involved determining the point at which the two components (steel + bronze) form a homogeneous solid mixture as a function of the milling time and the rotational speed. With regard to the rotational speed, it was found that a value of at least 300 rpm was necessary to obtain a homogeneous powder even at a milling time of 12 h. In contrast, even at very high milling times of 24 h, rotational speeds of 250 rpm resulted in a flake-like powder morphology in which individual bronze residues were still unmixed, similar to the tests with 6 h (Figs. 2a and 3: top-left). If the milling time is considered as the influencing factor, it can be seen in Fig. 2 that between 6 h to 12 h there is a limit representing the transition of an almost complete homogenization process during mechanical alloying. Steel-bronze powder mixtures milled at 300 rpm for 6 h show clear residues of unalloyed orange bronze particles in the optical microscopy images (Fig. 2a). In addition, the grain morphology has changed towards a very thin , flake-like structure with an average thickness of ~ 5 µm to

Table 3 Quantitative EDS-analysis of milled powder in Fig. 2c

	Cr	Fe	Ni	Cu	Sn
1	16.80	60.17	11.58	11.94	0.00
2	15.80	55.17	8.80	19.22	1.00
3	16.48	55.10	11.95	13.20	3.27

Elemental composition in wt%; normalized for the relevant alloying elements

Table 4 Comparison of the flowability of milled samples

Sample	Avalanche energy [kJ kg^{-1}]	Avalanche angle [°]
316L-Steel	10.45	35.2
300 rpm; 12 h	18.13	69.7
300 rpm; 12-12 h-int	8.48	55.5
400 rpm; 24 h	9.25	40.1

10 µm compared to the initial state in Fig. 1a. This structure resulted in a very sticky powder with an almost non-existent flowability in the milled end product. Accordingly, increasing the milling time to 12 h abruptly changes the composition and grain morphology. The light microscope image shown in Fig. 2b of a steel-bronze powder mixture, which was mechanically alloyed at 300 rpm and for 12 h, shows that from a certain point in the milling process, the grains change to a more rounded shape with no visible remnants of orange bronze particles. Furthermore, at this grinding time, the grain size distribution is very irregularly broadly scattered. Looking at the elemental composition at a grinding time of 12 h, it is clear from the EDS elemental analysis on three different metal particles (Fig. 2c and Table 3) that the mechanically alloyed powder was almost completely homogenized at these grinding parameters. In this regard, the quantitative analysis in Table 3 shows the distribution of copper, which is the main component of the bronze alloy, in the 316L steel particles. The Cu content of the three measured particles ranges from ~12 to 19 wt%. Considering that only 20 wt-% bronze was added to the steel powder, it appears that the relatively high solubility of copper is due to the Ni alloy component. In this two-substance system, complete solubility exists in the solid phase. This is also confirmed by measuring point 2 in Table 3 where a very high Cu content (19.22 wt%) is present to the expense of the Ni content (8.80 wt%).

To show the influence of milling parameters (rotation speed and time) on grain morphology, SEM images were taken of four different mechanically alloyed powders, each produced with different milling parameters (Fig. 3). As already shown in Fig. 2, if the kinetic energies are too low due to a too low rotational speed or a too short milling time of maximum 6 h, non-flowable powders are formed, whose particle geometry is flaky and asymmetric. The structure of a flake-like loose powder is shown in Fig. 3 at the top left image. If the grinding time is increased to 12 h, the resulting powders become much more flowable and the grains take on a rounder shape. It should be noted that the powders milled at 300 rpm and for 12 h (Fig. 3: top right) still show a very irregular particle size distribution. This changes when the milling parameters are further adjusted. Here, a change to intermittent operation has proven to be advantageous. Powders that were processed in an alternating milling process with 1 h pause time and 1 h rotation time showed a clearly more homogeneous particle size distribution in the left-bottom picture. Finally, a further increase of the rotation speed to the maximum value of 400 rpm and an increase of the grinding time to 24 h lead to a further improvement of the grain morphology. In the lower right picture it can be seen that the grain geometry now has become more spherical and the grain size distribution is also more homogeneous.

3.2 Dynamic flowability and particle size distribution

In order to compare the dynamic flowability of the milled powders with that of the steel powder, the avalanche energy and avalanche angle of the samples from Fig. 3 were consulted. Since the 300 rpm, 6 h sample was highly viscous and sticky, a measurement could not be made here. The evaluation of this direct comparison is shown in Table 4. It can be seen that a milling process at 300 rpm for 12 h results in a powder whose flowability is nearly twice that of the spherical

316L steel powder (18.13 kJ kg^{-1}; 69.7 °). Only a change of the milling process to interval operation with hourly breaks of one hour and reversal of direction leads to an improvement of the flow behavior. It should be noted that the avalanche energy is just below the steel powder (8.48 kJ kg^{-1}), but the avalanche angle is only insignificantly reduced (55.5 °). In conclusion, the flowability of the milled powder at the maximum rotational speed of 400 rpm and 24 h reaches approximately the Avlanche angle of the steel powder (40.1 °). In this context, it can be assumed that higher kinetic energies in the milling process and the resulting stronger cold deformation lead to more favorable particle shapes and thus better flow behavior.

In order to assess the usability of the powder obtained in the HEBM process for PBF-LB/M printing in terms of particle size distribution and fine particle content, the size distributions of two milled powder samples were compared with those of the starting powders (Fig. 4). Looking at the starting materials, it can be clearly seen that the bronze powder has a very broad particle size distribution with a high proportion of fine particles down to approx. 5 µm (Fig. 4b). In contrast, the steel powder has a rather narrow size distribution with a maximum particle size fraction of 50 µm to 60 µm, according to the manufacturer's specifications (Fig. 4a). A close examination of the two mechanically alloyed powder samples shows that their particle size distribution is significantly narrower than that of the bronze powder and has a similar Gaussian distribution to the steel powder (Fig. 4c and d). Furthermore, the fine particle content of the milled powders is not significantly higher than that of the steel powder. However, the distribution maximum for milled powders is visibly shifted towards the coarser grain fraction (approx. 65 µm to 88 µm).

3.3 Analysis of the crystal structure

In order to investigate the processes of solid solution formation and the formation of amorphous or nanocrystalline phases at the level of the crystalline structure, which occur during mechanical alloying, diffraction spectra of the raw materials (steel and bronze) and of a mixed-only powder fraction were measured first. These spectra (Fig. 5a) were used as reference for the interpretation of the high energy milled powder fractions.

The XRD pattern in Fig. 5a, which represents a section of the measured 2θ angular range from approx. 40° to 75°, indicates a face-centered cubic crystal system with very close lattice constants for both starting materials. The fact that the crystal structure of both substances are very similar is also shown by the spectrum of both materials in the mixed state. Here it can be seen that the diffraction peaks of the steel and the bronze partially overlap, which on the one hand leads to a broadening of the peaks and on the other hand results in two maxima. Due to the presence of an unalloyed mixture, the left peak maxima are still clearly attributable to the bronze component, whereas the right peak maxima

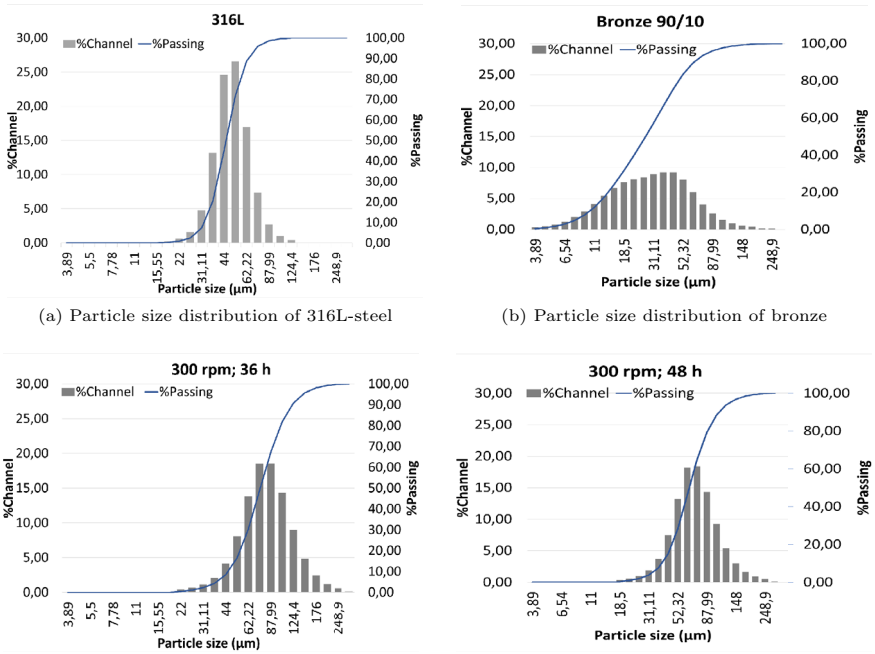

(a) Particle size distribution of 316L-steel

(b) Particle size distribution of bronze

(c) Particle size distribution of sample 300 rpm; 36h

(d) Particle size distribution of sample 300 rpm; 48h

Fig. 4 Comparison of the particle size distribution of milled samples

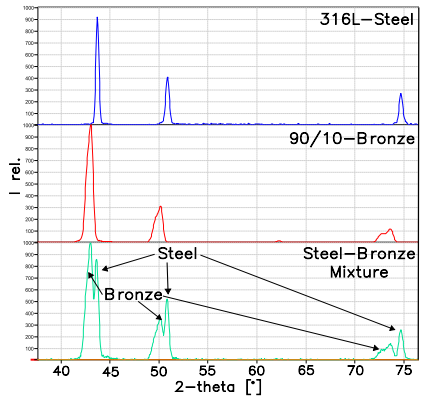

(a) Diffraction spectrum of the raw materials and the mixed powder

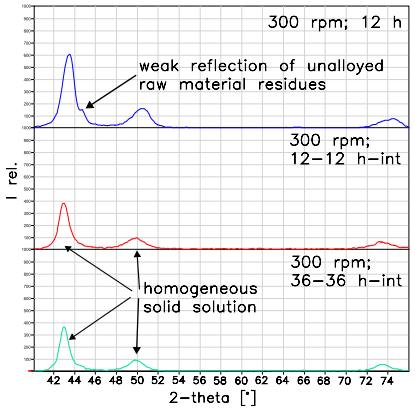

(b) Diffraction spectrum of the high energy milled powder

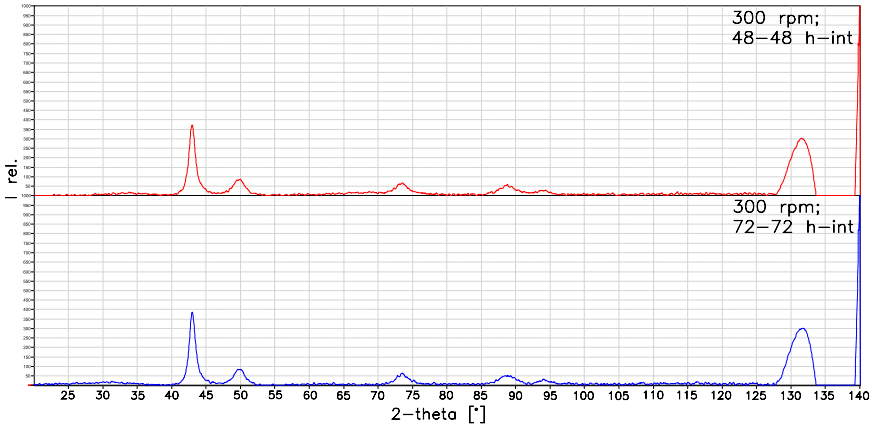

(c) Diffraction spectrum of the high energy milled powder at high process times

Fig. 5 Crystal structure analysis of mechanically alloyed powders

represent the steel component. This appearance of the XRD-spectrum changes seriously after high-energy milling of the steel-bronze powders. Looking at the measured diffraction spectra in Fig. 5b, it can be seen that at a rotational speed of 300 rpm and a milling time of 12 h, only the high-intensity peak at 43° still shows a weak indication of the presence of both crystal structures (steel and bronze). The other two weaker peaks at 50° and 73°, on the other hand, are present as single diffraction reflections. This strongly suggests that solid solution formation has not yet been fully completed due to the short milling time of 12 h. From this, the solid solution formation of both powder components improves when the ball mill is operated in interval mode with direction reversal (see Fig. 5b: middle spectrum). Although here the effective milling time is 12 h in absolute terms, just as in the upper spectrum, the hourly interruption of the milling process with a one-hour pause time seems to have a positive effect on the solid solution formation. However, a further increase of the process time to 36 h–36 h interval operation does not lead to any further change in the crystal structure (Fig. 5b: lower spectrum).

Finally, it was investigated whether structural properties in the powder change during very long mechanical alloying. For this reason, a diffractogram of a powder milled at 48 h and at 72 h in interval operation is shown in Fig. 5c in each case. The studies on the formation of amorphous phases during high-energy milling presented in the state of the art in Sect. 1 are not confirmed for the present steel-bronze alloy. This can be verified mainly from the fact that the XRD-spectrum (Fig. 5c) of the powder milled at 72 h shows no amorphous halo at low 2-θ angular regions.

3.4 Thermal analysis

To verify the primary objective of modifying the melting range as well as the melting behavior for better processability of DMMC materials in LBPF 3D printing in mechanically alloyed steel-bronze powder blends, such high-energy milled powder samples were subjected to thermal analysis from room temperature to 1550 °C. Fig. 6 shows an exemplary DTA evaluation of a powder sample which was mechanically alloyed in interval operation with 300 rpm and 48 h–48 h. During

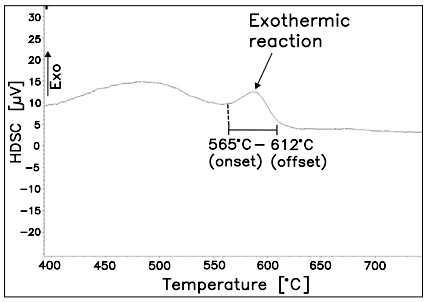

(a) Evaluation of the exothermic peak

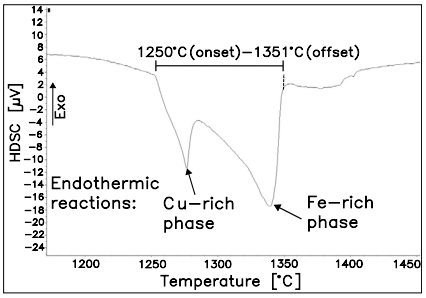

(b) Evaluation of the endothermic peak (melting range)

Fig. 6 Exemplary thermal analysis of a powder sample mechanically alloyed in interval operation with 300 rpm at 48 h–48 h

heating, a weak but distinct exothermic peak (Fig. 6a) first appeared in a temperature range from 550 °C to 650 °C for all milled samples that exhibited approximately completed solid solution formation (see Sect. 3.3). Since the presence of amorphous structures could be excluded in the crystal structure analysis in Fig. 5c, a possible exothermic crystallization of the material in the solid phase cannot be assumed. It is much more likely that the high plastic deformation energy during high-energy milling promotes the formation of metastable solid solution phases, which are converted back into a thermodynamically stable state when sufficiently heated (540 °C to 620 °C). Also possible would be the formation of metal carbides or, due to the existence of numerous alloying elements such as Ni, Cr and Sn the formation of intermetallic phases. More detailed explanations of this special thermal behavior of the mechanically alloyed powders are presented in Sect. 3.5.

Looking at the thermal analyses from temperatures of 1250 °C, the DTA curves for all homogeneous mechanically alloyed steel-bronze mixtures present as solid solution show two endothermic melting peaks occurring immediately after each other (Fig. 6b), with a much wider melting interval than the pure 316L steel powder. The melting peak at lower temperatures can therefore be attributed to the formation of a copper-rich phase, whereas the peak occurring at higher temperatures corresponds to the melting of an iron-rich phase. Finally, if the melting intervals of all mechanically alloyed powder samples are compared with the pure 316L steel raw powder (Table 5), it becomes clear that, on the one hand, the melting range of the milled powders is about three times higher than that of the 316L steel, and, on the other hand, the offset temperatures (corresponding to the liquidus temperature) of the milled powders are almost consistently about 100 °C lower. Taking into account that both solidus and liquidus temperatures can be significantly lowered for high energy milled steel-bronze powders, it can be noted that the basic objective of lowering the melting temperature of 316L steel by mechanical alloying with bronze has been achieved. In contrast, the influence of higher milling times on the melting point reduction seems to be insignificant.

3.5 Heat treatment and remelting

The following investigations take place against the background of making such mechanically alloyed powder mixtures, modified in the direction of lower melting ranges, usable for the PBF-LB/M 3D printing process for the production of diamond-metal matrix composites (DMMCs). In order to analyze in more detail the material behavior of mechanically alloyed steel-bronze powders during heating and melting, which differs from that of unalloyed powder blends, further crystallographic as well as SEM and elemental analyses (EDS) are carried out in the following Chapter on a heat-treated and remelted powder sample which was milled at 300 rpm and in interval operation (48 h–48 h).

Table 5 Melting ranges of mechanically alloyed samples

Sample	Onset [°C]	Offset [°C]
316L-Steel (raw material)	1412	1446
300 rpm; 12 h	1255	1360
400 rpm; 24 h	1256	1350
300 rpm; 12-12 h-int	1252	1346
300 rpm; 36-36 h-int	1257	1357
300 rpm; 48-48 h-int	1250	1351

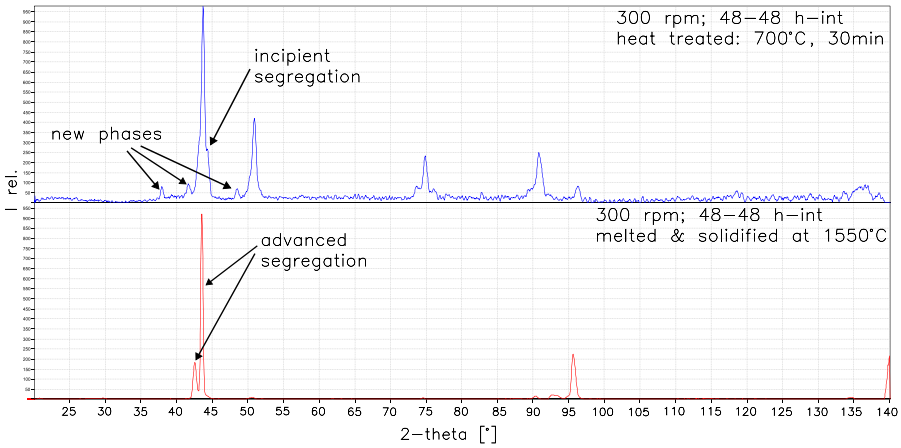

(a) Diffraction spectrum of heat-treated and melted powder samples

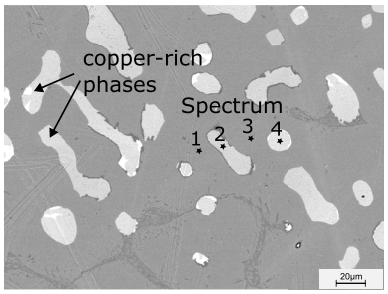

(b) SEM microscopy of melted (max. 1500 °C for 5 min) and solidified powder sample (with EDS measuring points)

Fig. 7 Investigation of heat treatment and melting/solidification behavior of mechanically alloyed powders processed at 300 rpm and 48–48h-int

First, the exothermic reaction described on the basis of the DTA-analyses in Sect. 3.4, Figure 6a will be investigated in the temperature range from 550 °C to 650 °C. For this purpose, mechanically alloyed powder samples heat-treated at 700 °C for 30 min were analyzed in the X-ray diffractometer. The diffraction spectrum in Fig. 7a (upper graph) confirms the assumptions made in Sect. 3.4, that it could be both the transformation of metastable phases and the formation of new phases such as carbides or intermetallic compounds. The direct comparison of this spectrum with the initial powder mixture in Fig. 5a shows the presence of three new peaks at $2\theta = 37.9°$, $2\theta = 41.7°$ and $2\theta = 48.5°$ which is an indication for new carbide or intermetallic phases. In addition, the main peak of the fcc solid solution ($2\theta = 43.6°$ in Fig. 7a: upper graph) shows the formation and splitting off of a second peak, indicating the beginning segregation of copper and tin-rich phases. Accordingly, the assumption that the exothermic reaction in the thermal analysis (Fig. 6a) represents the transformation of a metastable solid solution phase into two more stable phases (segregation) may well be correct. This is additionally confirmed by further consideration of the processes involved in the melting and solidification of the mechanically alloyed powder. The XRD-analysis of a remelted powder sample from the DTA measurement (Fig. 7a:lower graph) shows the same main peak at $2\theta = 43.6°$ in a clearly advanced segregated state. This segregated state after melting is finally verified by scanning electron microscopy of the solidified microstructure with material contrast and EDS elemental analysis (Fig. 7b + Table 6). Here, clear copper- and tin-rich precipitates can be seen in the steel structure, which are sharply distinguished from the surrounding iron-rich structure. The elemental analysis additionally confirms

Table 6 Quantitative EDS-analysis of melted powder in Fig. 7b

	Cr	Fe	Ni	Cu	Sn
1	15.14	62.99	12.74	9.14	0.00
2	0.71	4.36	4.52	81.78	8.63
3	14.53	61.52	11.69	12.27	0.00
4	0.46	2.62	2.87	79.36	14.69

Elemental composition in wt%; normalized for the relevant alloying elements

that the main part of the copper and tin previously dissolved in the milled steel powder has segregated as a separate precipitate after melting and solidification with a fraction of ~80 wt% Cu and ~8–15 wt% Sn. The strong attenuation and disappearance of the other fcc peaks (Fig. 7a: lower graph) otherwise present in the measured powder diffractograms at about $2\theta = 51.0°$, $2\theta = 74.8°$, and $2\theta = 90.8°$ can be explained by the fact that the measured melt drop had a very small metallographic cross section of only 3 mm to 4 mm. A simultaneously high crystallite size finally led to a grain structure which in this case did not fulfill the Bragg condition throughout for all net planes.

4 Conclusion

With regard to the initial objective of modifying 316L steel powder with bronze additions in such a way that the melting range of the alloy obtained is significantly lower than that of pure steel powder, it can be seen that such powder modifications by means of high-energy ball milling (HEBM) result in a melting onset that is about 150 °C to 160 °C lower. It could also be determined from thermal analyses (Sect. 3.4) that the melting interval increases from 35 °C for pure stainless steel to approx. 100 °C for mechanically alloyed steel-bronze blends.

Further important insights into the material characteristic processes of mechanical alloying of this 316L bronze composition could also be obtained:

- A parameter study for the mechanical alloying of this powder mixture was able to determine at which rotational speed and grinding time a homogeneous mixture of 316L steel and bronze is formed (300 rpm; 12 h). Further, it could also be verified by XRD-analysis that a face-centered cubic solid solution is present when these milling parameters are reached and exceeded.
- The grain morphology of the milled powder becomes increasingly spherical and the grain size distribution increasingly homogeneous during milling processes in interval operation and at higher milling parameters (400 rpm; 24 h).
- Long-term milling tests at 24 h and show an improvement in dynamic flowability almost approaching the material properties of 316L steel powder. In addition, milling tests at 36 h to 48 h do not lead to an increased formation of fine particles. Instead, the particle size distribution seems to shift towards higher average particle sizes.
- Combined investigations by means of thermal analysis (DTA), XRD-analysis, SEM-analysis and EDS elemental analysis revealed that when the powder is heated above 550 °C to 650 °C, an exothermic reaction takes place, which most likely indicates a segregation process. This segregation process occurred completely after the melting and solidification of the mechanically alloyed powders. This is proven by the closer analyses of the remelted steel-bronze structure (SEM + EDS), in which copper-rich and iron-rich phases are clearly present separately.

In summary, both the lowered melting range and the segregation process of Cu-rich phases after melting could lead to better processing of such modified DMMC base powders in an PBF-LB/M 3D printing process. In particular, the demonstrated formation of low-melting copper phases in the steel structure could minimize the susceptibility to cracking and pore formation. More detailed investigations on this will be addressed in further work.

Author contributions MPF: Conceptualization, methodology, validation, formal analysis, investigation, resources, writing—original draft, writing—review and editing, visualization, supervision. WT: Conceptualization, methodology, writing—review and editing, supervision and project administration.

Funding Open Access funding enabled and organized by Projekt DEAL. This work was funded by the Deutsche Forschungsgemeinschaft (DFG, German Research Foundation) [Grant Number TI 343/189-1].

Data availability All data regarding the parameters for the high energy ball milling and the settings of the analyzing instruments are available in Sect. 2.

Code availability Not applicable.

Declarations

Ethics approval and consent to participate Not applicable.

Consent for publication Not applicable.

Competing interests The authors declare that they have no competing interests.

References

1. Ozcelik Y, Yilmazkaya E. The effect of the rock anisotropy on the efficiency of diamond wire cutting machines. Int J Rock Mech Min Sci. 2011;48(4):626–36. https://doi.org/10.1016/j.ijrmms.2011.04.006.
2. Dwan JD. Production of diamond impregnated cutting tools. Powder Metall. 1998;41(2):84–6. https://doi.org/10.1179/pom.1998.41.2.84.
3. Tillmann W, Klaassen M. Dry holes call for diamond drills without coolant. Met Powder Rep. 2005;60(6):22–6. https://doi.org/10.1016/S0026-0657(05)70432-X.
4. Denkena B, Grove T, Bremer I, Behrens L. Design of bronze-bonded grinding wheel properties. CIRP Ann. 2016;65(1):333–6. https://doi.org/10.1016/j.cirp.2016.04.096.
5. Constantin L, Kraiem N, Wu Z, Cui B, Battaglia J-L, Garnier C, Silvain J-F, Lu YF. Manufacturing of complex diamond-based composite structures via laser powder-bed fusion. Addit Manuf. 2021;40:101927. https://doi.org/10.1016/j.addma.2021.101927.
6. Spierings AB, Leinenbach C, Kenel C, Wegener K. Processing of metal-diamond-composites using selective laser melting. Rapid Prototyp J. 2015;21(2):130–6. https://doi.org/10.1108/RPJ-11-2014-0156.
7. Wegner J, Fehr A, Platt S, Kleszczynski S, Witt G, Tillmann W. Diamond-impregnated 316l metal matrix composites fabricated by powder bed fusion with laser beam-influences of the energy input on the microstructural properties. Diam Relat Mater. 2020;109:108040. https://doi.org/10.1016/j.diamond.2020.108040.
8. Artini C, Muolo ML, Passerone A. Diamond-metal interfaces in cutting tools: a review. J Mater Sci. 2012;47(7):3252–64. https://doi.org/10.1007/s10853-011-6164-6.
9. Tillmann W, Ferreira M, Steffen A, Rüster K, Möller J, Bieder S, Paulus M, Tolan M. Carbon reactivity of binder metals in diamond-metal composites-characterization by scanning electron microscopy and X-ray diffraction. Diam Relat Mater. 2013;38:118–23. https://doi.org/10.1016/j.diamond.2013.07.002.
10. Steffen A. Untersuchung der Diamant-Metall-Grenzfläche in Diamantverbundwerkstoffen. Technische Universität Dortmund. 2013. https://doi.org/10.17877/DE290R-5728.
11. Tillmann W, Tolan M, Pinho Ferreira M, Paulus M, Becke M, Stangier D. X-ray diffraction (xrd)-studies on the temperature dependent interface reactions on hafnium, zirconium, and nickel coated monocrystalline diamonds used in grinding segments for stone and concrete machining. Materialwiss Werkstofftech. 2016;47(12):1193–201. https://doi.org/10.1002/mawe.201600713.
12. Kovalenko V, Golovko L, Meijer J, Anyakin M. New developments in laser sintering of diamond cutting disks. CIRP Ann. 2007;56(1):189–92. https://doi.org/10.1016/j.cirp.2007.05.046.
13. Koptyug A, Popov VV, Botero Vega CA, Jiménez-Piqué E, Katz-Demyanetz A, Rännar L-E, Bäckström M. Compositionally-tailored steel-based materials manufactured by electron beam melting using blended pre-alloyed powders. Mater Sci Eng A. 2020;771:138587. https://doi.org/10.1016/j.msea.2019.138587.
14. Ron T, Leon A, Popov V, Strokin E, Eliezer D, Shirizly A, Aghion E. Synthesis of refractory high-entropy alloy wtamonbv by powder bed fusion process using mixed elemental alloying powder. Materials. 2022;15(12):4043. https://doi.org/10.3390/ma15124043.
15. Popov VV, Grilli ML, Koptyug A, Jaworska L, Katz-Demyanetz A, Klobčar D, Balos S, Postolnyi BO, Goel S. Powder bed fusion additive manufacturing using critical raw materials: a review. Materials. 2021;14(4):909. https://doi.org/10.3390/ma14040909.
16. Spriano S, Chen Q, Settineri L, Bugliosi S. Low content and free cobalt matrixes for diamond tools. Wear. 2005;259(7–12):1190–6. https://doi.org/10.1016/j.wear.2005.02.076.
17. Kamphuis B. Diamond technology - cobalt and nickel free bond powder for diamond tools: Cobalite cnf - a paper on the increased use of pre-alloyed micron size metal powders in diamond toolmaking, that now constitute around 20% of the total market. Ind Diam Rev. 2004;1:26–33.
18. Zeren M, Karagöz Ş. Sintering of polycrystalline diamond cutting tools. Mater Des. 2007;28(3):1055–8. https://doi.org/10.1016/j.matdes.2005.09.018.
19. Rosa LG, Fernandes JC, Anjinho CA, Coelho A, Amaral PM. Long-term performance of stone-cutting tools. Int J Refract Metals Hard Mater. 2015;49:276–82. https://doi.org/10.1016/j.ijrmhm.2014.05.021.
20. Christudasjustus J, Witharamage CS, Walunj G, Borkar T, Gupta RK. The influence of spark plasma sintering temperatures on the microstructure, hardness, and elastic modulus of the nanocrystalline al-xv alloys produced by high-energy ball milling. J Mater Sci Technol. 2022;122:68–76. https://doi.org/10.1016/j.jmst.2022.02.008.
21. Esteves L, Christudasjustus J, O'Brien SP, Witharamage CS, Darwish AA, Walunj G, Stack P, Borkar T, Akans RE, Gupta RK. Effect of V content on corrosion behavior of high-energy ball milled aa5083. Corros Sci. 2021;186:109465. https://doi.org/10.1016/j.corsci.2021.109465.

22. Kovalev DY, Kochetov NA, Chuev II. Fabrication of high-entropy carbide (TiZrHfTaNb)C by high-energy ball milling. Ceram Int. 2021;47(23):32626–33. https://doi.org/10.1016/j.ceramint.2021.08.158.
23. Câmara NT, Raimundo RA, Lourenço CS, Morais LMF, Silva DDS, Gomes RM, Morales MA, Macedo DA, Gomes UU, Costa FA. Impact of the sic addition on the morphological, structural and mechanical properties of cu-sic composite powders prepared by high energy milling. Adv Powder Technol. 2021;32(8):2950–61. https://doi.org/10.1016/j.apt.2021.06.006.
24. Dudina DV, Grigoreva TF, Kvashnin VI, Devyatkina ET, Vosmerikov SV, Ukhina AV, Novoselov AN, Legan MA, Esikov MA, Lukyanov YL, Anisimov AG, Kovaleva SA, Lyakhov NZ. Microstructure and properties of cu-10 wt% al bronze obtained by high-energy mechanical milling and spark plasma sintering. Mater Lett. 2022;312:131671. https://doi.org/10.1016/j.matlet.2022.131671.
25. Huang M, Jiang J, Wang Y, Liu Y, Zhang Y. Effects of milling process parameters and pcas on the synthesis of al0.8co0.5cr1.5cufeni high entropy alloy powder by mechanical alloying. Mater Design. 2022;217:110637. https://doi.org/10.1016/j.matdes.2022.110637.
26. Zhang Z, Wang Q, Mu D, Shen G, Liu M, Zhang M, Chan SLI, Liang J, Wang J. Microstructure evolution and mechanical properties of cocrfenial03 high entropy alloy produced by ball milling in combination with thermomechanical consolidation. Mater Character. 2022;187:111833. https://doi.org/10.1016/j.matchar.2022.111833.
27. Ozdemir F, Witharamage CS, Darwish AA, Okuyucu H, Gupta RK. Corrosion behavior of age hardening aluminum alloys produced by high-energy ball milling. J Alloy Compd. 2022;900:163488. https://doi.org/10.1016/j.jallcom.2021.163488.
28. Takenaka K, Setyawan AD, Sharma P, Nishiyama N, Makino A. Industrialization of nanocrystalline fe-si-b-p-cu alloys for high magnetic flux density cores. J Magn Magn Mater. 2016;401:479–83. https://doi.org/10.1016/j.jmmm.2015.10.091.
29. Akase Z, Kimura K, Saito T, Niitsu K, Tanigaki T, Iwasaki Y, Sharma P, Makino A, Shindo D. Magnetic flux in soft magnetic fe-si-b-p-cu amorphous alloy containing nanocrystallites analyzed by electron holography. J Magn Magn Mater. 2022;541:168519. https://doi.org/10.1016/j.jmmm.2021.168519.
30. Motozuka S, Sato H, Kuwata H, Bito M, Okazaki Y. Effects of interfacial interactions between metal and process control agents during ball milling on the microstructure of the milled fe-based nanocrystalline alloy powder. Heliyon. 2022. https://doi.org/10.1016/j.heliyon.2022.e10325.
31. Chattopadhyay PP, Manna I. Effect of partial substitution of cu in al 65 cu 35 by transition metal in mechanical alloying of al 65 cu 20 tm 15. Mater Manuf Processes. 2002;17(5):583–94. https://doi.org/10.1081/AMP-120016084.
32. Tan Z, Xue YF, Wang L, Cheng XW, Zhang L, Zhang HF, Wang AM. Alloying evolution and stability of al 65 cu 20 ti 15 during process of amorphisation by high energy ball milling. Powder Metall. 2012;55(5):361–7. https://doi.org/10.1179/1743290112Y.0000000005.
33. Tan Z, Wang L, Xue Y, Cheng X, Zhang L. Structural modification of al65cu16.5ti18.5 amorphous powder through annealing and post milling: improving thermal stability. J Mater Sci Technol. 2016;32(12):1326–31. https://doi.org/10.1016/j.jmst.2016.03.007.
34. Dutkiewicz J, Jaworska L, Maziarz W, Czeppe T, Lejkowska M, Kubíček M, Pastrňák M. Consolidation of amorphous ball-milled zr-cu-al and zr-ni-ti-cu powders. J Alloy Compd. 2007;434–435:333–5. https://doi.org/10.1016/j.jallcom.2006.08.201.
35. Seidel M, Reibold M, Bächer I, Bauer H-D, Eckert J, Schultz L. Progress of solid-state reaction during mechanical alloying of zr-al-cu-ni bulk metallic glass-forming alloys. Materials Science and Engineering: A. 1997;226–228:383–7. https://doi.org/10.1016/S0921-5093(96)10648-1.
36. Djakonova NP, Sviridova TA, Zakharova EA, Molokanov VV, Petrzhik MI. On the synthesis of zr-based bulk amorphous alloys from glass-forming compounds and elemental powders. J Alloy Compd. 2004;367(1–2):191–8. https://doi.org/10.1016/j.jallcom.2003.08.036.
37. Junwei L, Jun L, Jun W, Shiqiang L, Muhai D. Microstructure and formation mechanisms of tininb amorphous powder prepared by mechanical alloying. Mater Lett. 2020;263:127158. https://doi.org/10.1016/j.matlet.2019.127158.
38. Xu Y, Zhou S, Liao B, Zhao S, Dai X, Chen D. Effect of milling time on the microstructure and magnetic properties of amorphous ti50fe50 alloys prepared by mechanical alloying. J Market Res. 2019;8(5):3929–35. https://doi.org/10.1016/j.jmrt.2019.07.001.